Theoretical study on the micro-scale oxidation of resin-infused carbon ablators

Joseph C. Ferguson[a], Francesco Panerai[b,*], Jean Lachaud[c], Nagi N. Mansour[d]

[a]*STC at NASA Ames Research Center, Mail Stop 258-6, Moffett Field, California, USA*
[b]*AMA Inc. at NASA Ames Research Center, Mail Stop 234-1, Moffett Field, California, USA*
[c]*C la Vie, University of New Caledonia, av. James Cook, Noumea, New Caledonia*
[d]*Advanced Supercomputing Division, NASA Ames Research Center, Mail Stop 258-5, Moffett Field, California, USA*

Abstract

When subjected to high enthalpy air, phenolic-impregnated carbon-based ablative thermal protection systems undergo oxidation of their carbon fiber substrate and carbonized phenolic matrix. The oxidation process is governed by the competition between reaction and diffusion within the porous material and occurs at a range of depths depending on the flow conditions, the material chemical composition, and the material micro-structure. This study aims to examine the effects of the distribution of carbonized phenolic matrix on the oxidation behavior of carbon fiber materials, with the goal of guiding future material design. The oxidation is simulated on ideal geometries and on representations of actual fibrous carbon preforms obtained from X-ray microtomography. Diffusion is simulated using a random walk technique with a linear interpolation method for surface collisions. Oxidation reactions are simulated using a sticking probability law. It is shown that the oxidation characteristics, particularly the oxidation depth, are strong functions of the Thiele number and that the effect of the matrix distribution within the fibers is more pronounced at low Thiele regimes.

---

[*] Corresponding author. Tel.: +1 (650) 604 3075.
Email address: `francesco.panerai@nasa.gov` (Francesco Panerai)

Preprint submitted to Carbon *June 4, 2017*

Nomenclature

Greek

ϵ	Porosity, -
Ω	Molar volume, $\mathrm{m}^3 \cdot \mathrm{mol}^{-1}$
Φ	Thiele number, -
ρ	Density, kg m^{-3}
θ	Average cylinder angle, rad

Symbols

A	Reactivity contrast, -
$\vec{e}$	Unit vector, -
C	Concentration, $\mathrm{mol} \cdot \mathrm{m}^{-3}$
D	Diffusion coefficient, $\mathrm{m}^{-2} \cdot \mathrm{s}^{-1}$
d	diameter, m
J	Molar oxidation flux, $\mathrm{mol} \cdot \mathrm{m}^{-2} \cdot \mathrm{s}^{-1}$
k	Reactivity, $\mathrm{m} \cdot \mathrm{s}^{-1}$
n	Surface normal, -
r	Radius, m
S	Surface function
s	Specific surface area, m^{-1}
t	Time, s
v	Recession velocity, $\mathrm{m} \cdot \mathrm{s}^{-1}$
x	Mass fraction, -
z	Matrix recession depth, m

Subscripts

eff	effective
f	fiber
m	matrix
p	pore

1. Introduction

Atmospheric entry missions require the use of thermal protection systems (TPS) to mitigate the aerothermal loads experienced at hypersonic conditions. One successful class of TPS materials are light-weight carbon phenolic ablators, built upon a carbon fiber preform and impregnated with phenolic resin. The phenolic impregnation improves mechanical properties [1] and limits oxygen penetration into the material. During entry, the phenolic resin pyrolyzes [2], causing a blow back of pyrolysis gases into the boundary layer. During pyrolysis, the phenolic resin undergoes carbonization, also referred to as charring, which produces a structure of pseudo-graphitic carbon left within the carbon fiber substrate. Depending on the impregnation and curing process of the phenolic resin, as well as the pyrolysis conditions, the carbonized resin can have a variety of distributions, densities, and mass fractions [3]. After full pyrolysis, the remaining carbonaceous material, composed of carbon fiber substrate and carbonized phenolic matrix, undergoes mass loss due to oxidation, sublimation, and spallation[4] (mass loss due to mechanical forces of friction and shear).

Many current ablation material response models, based on the work of Kendall et. al [5], rely on a surface ablation hypothesis. Heritage models do not account for the micro-structure of the material and the in-depth oxidation that can occur due to the diffusion of reactants into the material. Because of the high porosity and range of oxidation depths, the micro-scale oxidation behavior must be understood and incorporated into the next generation of volume averaged models [6] in order to guide material design.

A micro-scale oxidation model was first proposed by Lachaud and Vignoles [7] and applied to ideal representations of carbon fiber substrates [8]. Our research group then studied the inclusion of a phenolic phase on ideal representations of carbon fiber substrates in order to develop a preliminary understanding of the effects of resin distribution on the oxidation process [9]. However, such ideal geometries do not adequately capture the complex fiber clusters and structures evidenced in real carbon fiber substrates under a scanning electron microscope [10]. An effort was made to obtain a realistic representation of carbon fiber substrates through the use of hard X-ray micro-tomography [10, 11]. The resulting tomography images, with sub-micron voxel sizes, provide a digital representation of the real material that can be used to calculate material properties or simulate material response [12, 13]. A computational framework, called Porous Materials Analysis (PuMA) [14] was developed at the NASA Ames Research Center to handle these large micro-tomography datasets. PuMA includes an implementation of the oxidation method proposed by Lachaud and Vignoles [7], modified to oxidize large datasets using parallel computing.

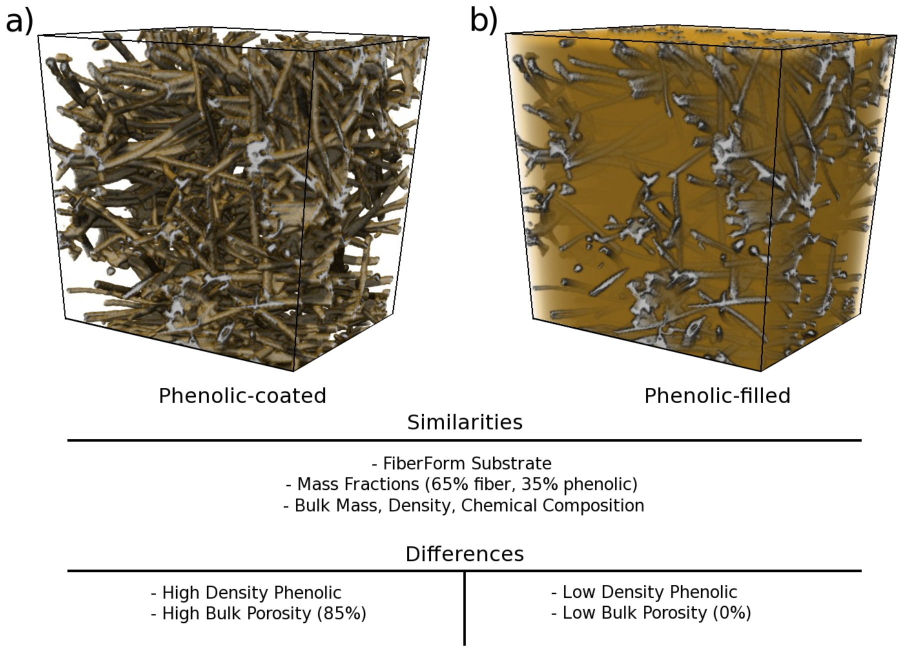

Figure 1: Visualization of two example materials: a) rigid carbon fiber preform coated with high density carbonized phenolic resin, and b) rigid carbon fiber preform filled with low density carbonized phenolic resin.

Using the PuMA framework, this study aims at understanding the effects of the micro-scale structure on the overall oxidation of resin-infused carbon fibers in order to guide material design. To this goal, we examine the effects of two carbonized phenolic distributions, shown in Fig. 1, on the micro-scale oxidation response. These two distributions, representing extreme cases, were selected: (a) carbon fiber substrate coated with a high density char and (b) carbon fiber substrate filled with a low density char. The overall mass of the charred material is the same in each case. The resulting materials, built upon the same carbon fiber substrate, have different porosity, but have the same constituent mass fractions, density, and chemical composition. These distributions are not intended to represent those of existing materials, but rather to serve as a theoretical model, capturing the extreme cases, to study the micro-scale oxidation and guide future material development.

Simulations are performed on ideal geometries as well as on micro-tomography representation of a carbon fiber preform material at various diffusion/reaction regimes for both the phenolic-coated (Fig. 1a) and phenolic-filled (Fig. 1b) cases.

Section 2 provides an overview of the simulation tools used in this study. We describe the oxidation model and the numerical method used to solve the diffusion/reaction problem. We also provide details on the use of 3D micro-tomography within the PuMA framework. Section 3 details analytical and numerical studies on ideal geometries, as well as numerical simulations on tomographic representations of a carbon fiber material available commercially (in this case FiberForm®). Section 4 contains the conclusion and outlook.

2. Methods

2.1. Physical model

For carbon/resin composites, the oxidation reaction of the carbonaceous char is a main source of material recession during ablation at temperatures below the sublimation regime. In an oxygen-rich entry plasma, oxidation primarily occurs via the reaction pathway $\mathrm{C(s)} + \mathrm{O} \longrightarrow \mathrm{CO}$ and, to a lesser extent, via $\mathrm{C(s)} + \mathrm{O_2} \longrightarrow \mathrm{CO_2}$ [15**?** , 16]. Other decomposition mechanisms may also occur under certain conditions, e.g. sublimation, nitridation, decomposition via reactions with $\mathrm{CO_2}$ and material removal by shear stresses. For a fibrous char, the local motion of the carbon/gas interface can be modeled using a differentiable surface function $S(x, y, z, t)$ [7, 8], as:

$$\frac{\partial S}{\partial t} + \vec{v} \cdot \nabla S = 0, \tag{1}$$

where the recession velocity, $\vec{v}$, of the surface is

$$\vec{v} = \Omega \, J \, \vec{n} \tag{2}$$

Here, Ω is the solid molar volume and $\vec{n}$ is the unit normal vector from the surface. J is the molar oxidation flux. Assuming Fickian mass diffusion and first order oxidation reactions, J is given by

$$J = -D\nabla C \cdot \vec{n} = k_f C \tag{3}$$

where D is the diffusion coefficient of the reactant in the bulk fluid phase, k_f is the intrinsic reactivity [17] of the carbon fiber[1], and $C = C(x, y, z, t)$ is the local concentration of oxygen.

The conservation of oxygen in the gas phase assuming negligible convection is given by

$$\frac{\partial C}{\partial t} - \nabla \cdot (D\nabla C) = 0 \tag{4}$$

An analogous expression to Eq. 3 can be written for the carbonized matrix, with the intrinsic reactivity of the matrix k_m used in place of k_f [7, 8]. The absolute values of k_f and k_m are very difficult to characterize, both experimentally and numerically, and a large scatter of data is found in the literature [17]. However, a ratio of 1:10 between the intrinsic reactivity of the carbon fibers (usually rayon- or PAN-based) and that of the matrix is a typical approximation [17], owing to the larger presence of atomic level defects in amorphous carbon.

Analytical solutions of Eqs. 1-4 in ideal porous media have shown that the oxidation process is controlled by two competing scales, namely the rate of diffusion of the reactants into the material and their rate of reaction at the surface[8]. This competition is quantified by the Thiele number, Φ, which for a single-phase fibrous medium can be defined as

$$\Phi = \frac{d_p}{\sqrt{D_{\text{eff}}/(s_f k_f)}} \tag{5}$$

Here, d_p is the mean pore diameter of the medium, D_{eff} is the effective diffusion coefficient, s_f is the specific surface area, and k_f is the reactivity of the fibers.

---

[1] The intrinsic reactivity of the carbon fiber is not to be confused with the effective reactivity, k_{eff}, which describes, instead, the reactivity of the bulk porous material

In the diffusion-limited regime, $\Phi \gg 1$, the high reaction to diffusion ratio yields oxidation that occurs at the first gas surface interface. Conversely, in the reaction limited regime, $\Phi \ll 1$, reactants are able to diffuse in depth into the material prior to oxidizing the surface. In the mixed regime, $\Phi \approx 1$, reactants are able to partially diffuse into the material prior to reacting.

The presented model uses a single mesoscopic reactivity value based on empirical relations[15]. A higher fidelity study of the material recession should consider the full set of heterogeneous reactions approximated in this reactivity model, including the transport of reaction products[18].

2.2. Numerical method

In order to solve the reaction/diffusion problem described by Eqs. 1-4 on complex porous media, a particle based simulation technique was proposed in [7], and later improved to be run in parallel on large tomography datasets [14]. Micro-tomography representations of the material (see section 2.4) are used as a computational domain and are stored as a 3D matrix of grayscale values that correspond to the local material density. Oxygen atoms are represented by particles, called walkers, whose diffusion towards and into the porous material is simulated through a Brownian motion technique [7]. Walkers are initially located in a buffer zone placed at the top of the computational domain, as shown in Fig. 2. A constant concentration of oxygen is maintained in the buffer zone during a simulation, satisfying a Dirichlet boundary condition. As the material recedes, the buffer zone is shifted in the direction of material recession so that the diffusion length to the surface remains constant throughout the simulation. Periodic boundary conditions are used at the side of the domain and a reflective (i.e. insulating) boundary condition on the bottom of the domain.

Surface collisions are determined based on a grayscale interpolation method [14] rather than in previous implementations [7] in which collisions were based on a triangle isosurface from a marching cubes algorithm [19]. Surface recession is simulated through a sticking probability law [7, 20]. In the case of a sticking event, the nearest material vertex in the global matrix is reduced by the grayscale attenuation rate [14]. In the case of a non-sticking collision, the walker is diffusely reflected at a random angle to complete its walk.

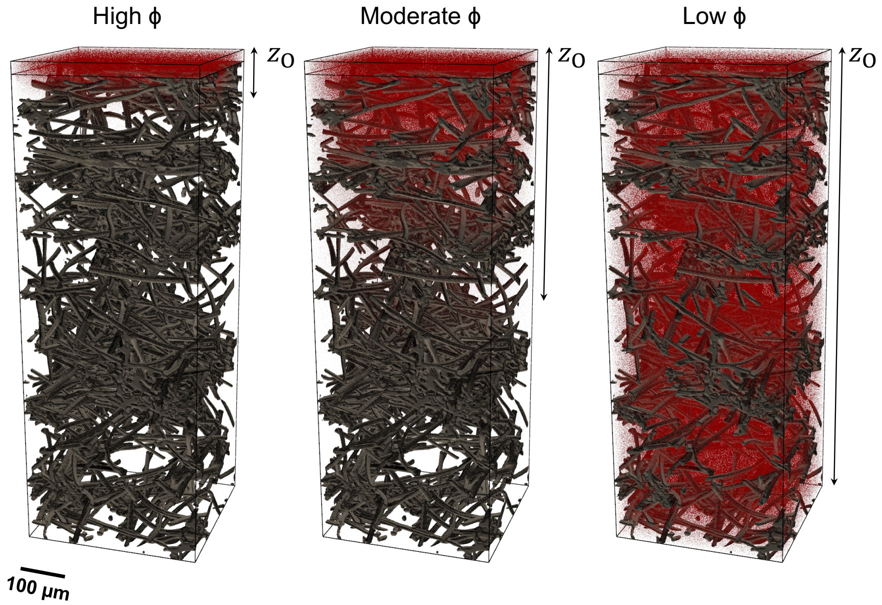

Figure 2: Example simulation domains in three Thiele regimes, showing the carbon fiber preform in gray, walkers in red, and the steady state oxygen diffusion depth, z_O. The buffer zone, populated with walkers at the top of the domain, is also displayed.

2.3. The PuMA simulation framework

The Porous Materials Analysis (PuMA) was developed to serve as a computational framework for calculating material properties and material response from micro-tomography data of porous materials [14]. The oxidation model and numerical method described in section 2.1 and section 2.2, respectively, were implemented into PuMA and were verified against analytical solutions [21].

The oxidation model was parallelized using OpenMP [22, 23] for multi-threaded simulations on a shared memory system. In the parallelization scheme, walkers are divided into walker groups, with each walker group assigned to a processor. The random walks are parallelized over the walker groups, with each group running independently over a predefined number of time steps, called a megastep. Each group maintains its initial oxygen concentration in the buffer zone for every time step; the aggregate of these conditions maintains the integrity of the Dirichlet boundary condition.

The speed increase scales approximately linearly with the number of processors available on a shared-memory system. Utilizing all 36 processors on the test machine, a 25 fold speed increase was observed. The parallelization of the oxidation model allows for the simulation of oxidation in the low Thiele regime on large datasets, which would otherwise have had prohibitively long run times.

2.4. Computational domains from X-ray micro-tomography

Micro-tomography has become a very useful tool for material science applications [12] [13], allowing for non-destructive characterization of a material microstructure at a sub-micron scale. For this study, X-ray micro-tomography imaging of FiberForm was performed at the Advanced Light Source (ALS) at Lawrence Berkeley National Laboratory [11]. FiberForm is the fibrous substrate of the Phenolic Impregnated Carbon Ablator (PICA), a state-of-the-art lightweight ablator with a record of successful use in several NASA missions. Details about micro-tomography imaging and reconstruction of FiberForm are provided in previous publications [10, 14]. A visualization example, obtained using a threshold-based marching cubes segmentation procedure implemented in PuMA is shown in Fig. 2. For the results presented in section 3, we used tomography volumes of 0.5 mm × 0.5 mm × 1 mm, with a voxel size of 1.3 μm. This voxel size provides an accurate resolution of the material microstructure [24].

As the purpose of this study is to examine the effects of charred resin distribution (the two extremes of which are shown in Fig. 1), attempts were made to use microtomography of impregnated samples of FiberForm, but were not successful due to the low density (and X-ray absorption) of the carbonized matrix. However, algorithms were developed to numerically add the matrix to the carbon fiber substrate. For the phenolic-coated case, fibers were coated with a matrix of approximately $r_m = \sqrt{2}r_f$, doubling the solid volume fraction of the domain. To create the matrix, intersecting spheres of the desired radius were created around each material edge voxel within the domain; the combination of these spheres resulted in a good approximation of a uniform coating. For the phenolic-filled case, the matrix was evenly distributed throughout the domain. Both the filling matrix and the coating matrix were given a mass fraction $x_m = 0.35$. Therefore, the density and chemical compositions of the bulk material remained unchanged for the two cases. The intrinsic density of the matrix phase in each case is found through the following mass balance:

$$\frac{\rho_m \epsilon_m}{x_m} = \frac{\epsilon_f \rho_f}{x_f} \tag{6}$$

where ρ is the density, ϵ is the volume fraction, and x is the mass fraction. The subscripts f and m denote fiber and matrix, respectively.

3. Results and discussion

3.1. Modeling of ideal geometries

In a previous work, an analytical solution of the steady state oxidation was derived for a fiber parallel to a reactant concentration gradient, surrounded by a matrix of higher reactivity [21]. This analytical model provides the shape and height of the oxidized fiber at combinations of matrix-to-fiber reactivity contrast A (defined later) and Sherwood number. The analytical solution was used in [14] as a verification of the oxidation model implemented in PuMA. As the present study focuses on transverse isotropic fibrous media, we extended the analytical solution to an array of infinite, parallel cylinders perpendicular to the reactant concentration gradient, which more closely resembles the properties of the actual material. Figure 3 shows a single fiber isolated from the two ideal geometries analyzed: cylindrical fibers coated by a high density matrix layer and cylindrical fibers immersed in a uniform low density matrix that occupies the entire void space. The two cases are referred to as "matrix-coated" and "matrix-filled", respectively.

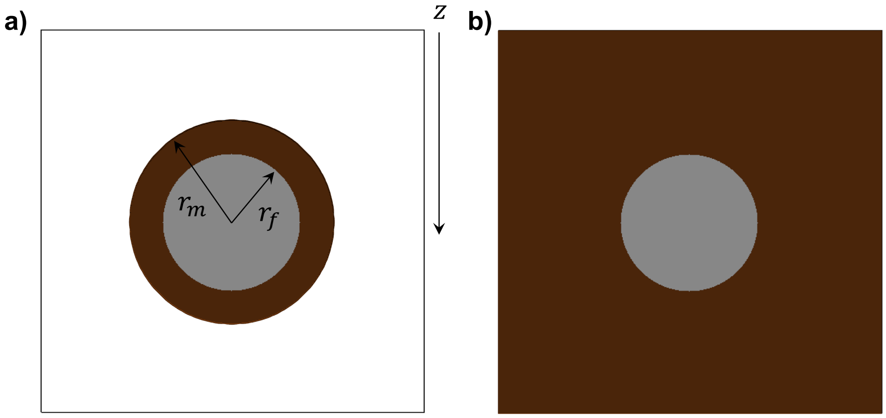

Figure 3: Schematic of single fiber isolated from ideal geometries considered in this study: a) fibers coated with high density matrix, and b) fibers filled with a uniform low density matrix. Fiber and matrix are displayed in gray and brown colors respectively.

For the two geometries of Fig. 3, one can write [8]:

$$\frac{d\vec{r}_f}{dt} = -\Omega_f k_f C_z \vec{e}_r \tag{7}$$

for the recession velocity of the fiber, and

$$\frac{d\vec{r}_m}{dt} = -\Omega_m k_m C_z \vec{e}_r \tag{8a}$$

$$\frac{d\vec{z}}{dt} = \Omega_m k_m C_z \vec{e}_z \tag{8b}$$

for the recession velocity of the matrix for the cases of Fig. 3a and Fig. 3b. $\vec{e}$ is the unit vector of the orientation of the surface. C_z is the concentration of the reactant at depth z and is assumed to be uniform in the x-y plane. Although Eqs. 7-8b are valid at every Thiele regime, the exact value of C_z is only known for a reaction-limited case, where the concentration at every point can be assumed to be equal to the concentration in the buffer zone, C_0.

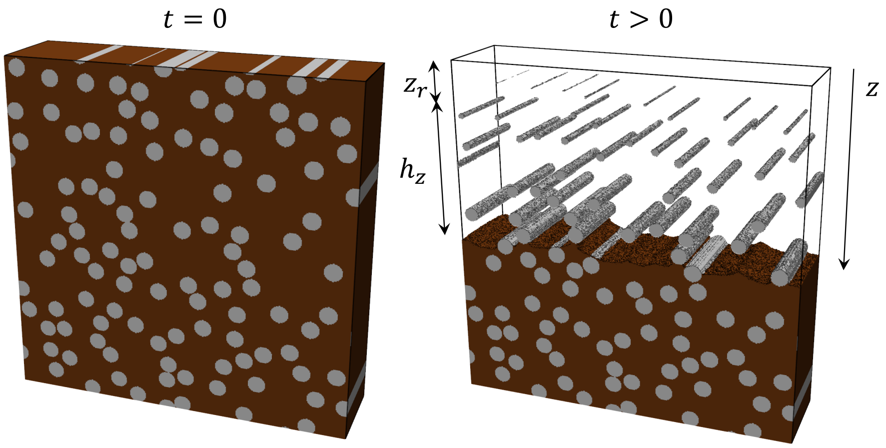

Figure 4: Schematic of randomly positioned cylinders perpendicular to the reactant concentration gradient prior to (left) and during (right) oxidation.

For the matrix-filled case in the low Thiele regime, an approximate analytical solution for the steady-state reaction depth can be found from Eq. 7 and Eq. 8b. As shown in Fig. 4, we define z and z_r as the depth of matrix and fibers recession front, respectively. For an infinite random array of cylinders, z_r becomes the depth of the midpoint of the highest cylinder that has not fully receded. The overall recession depth becomes $h_z = z - z_r$. The depth of the matrix at time t is found by integrating Eq. 8b from 0 to t and assuming that the matrix recedes uniformly in z:

$$z(t) = \Omega_m k_m C_0 t \tag{9}$$

For the fibers, it is assumed that each cylinder recedes uniformly in the radial direction and only begins receding when the matrix has passed the midpoint of the given cylinder. This assumption holds approximately true for A > 2, where A is the matrix-to-fiber reactivity contrast, $\mathrm{A} = \Omega_m k_m / \Omega_f k_f$.

We define t_r to be the time for the matrix to reach the midpoint of the highest fiber that has not fully receded. From Eq. 9, t_r is found to be

$$t_r = \frac{z_r}{\Omega_m k_m C_0} \tag{10}$$

The radius of the highest cylinder that has not fully receded is found by integrating Eq. 7 from t_r to t. Hence, we have:

$$r_f(t) = r_{f,0} \qquad \text{for } t \leq t_r \tag{11a}$$

$$r_f(t) = r_{f,0} - \Omega_f k_f C_0 (t - t_r) \text{for } t > t_r \tag{11b}$$

From Eq. 11b, the matrix depth below the highest cylinder can then be obtained by computing t and t_r from Eq. 9:

$$r_f(t) - r_{f,0} = -\frac{\Omega_f k_f}{\Omega_m k_m}(z - z_r) \tag{12}$$

or

$$h_z(t) = A(r_{f,0} - r_f(t)) \tag{13}$$

At steady-state, where $\frac{dz}{dt} = \frac{dz_r}{dt}$ and the radius of the highest cylinder approaches 0, Eq. 13 becomes

$$h_z^{\perp} = \mathrm{A} r_{f,0} \tag{14}$$

This solution is valid for $\mathrm{A} \gg 1$. For fibers parallel to the reactant concentration gradient, fully surrounded by a reactive matrix, it has been shown in [21] that the steady state height of the fiber is calculated as:

$$h_z^{\parallel} = r_{f,0}\sqrt{\mathrm{A}^2 - 1} \tag{15}$$

Interpolating between Eq. 14 and Eq. 15 , an approximate solution for the reaction depth of randomly oriented cylinders is found to be:

$$h_z = \left(\frac{2\theta}{\pi}\right) r_{f,0}\sqrt{A^2 - 1} + \left(1 - \frac{2\theta}{\pi}\right) r_{f,0} A \tag{16}$$

where θ is the average magnitude of the angle between the cylinders and the perpendicular plane, $\theta \in [0, \pi/2]$. For $\mathrm{A} \gg 1$, the solution converges to Eq. 14.

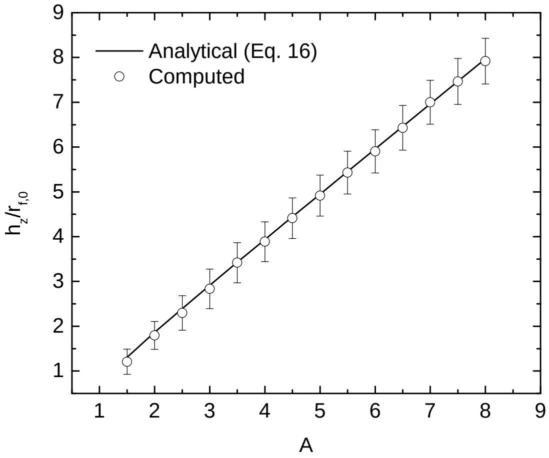

Figure 5: Comparison between the analytical solution in Eq. 16 and PuMA simulations in the low Thiele regime at increasing reactivity contrasts A, performed using a digital carbon/phenolic composite with randomly-oriented cylindrical fibers.

Figure 5 shows the steady state reaction depth for randomly oriented cylinders ($\theta = \pi/4$) in the low Thiele regime as a function of the reactivity contrast. The tested geometries had a porosity $\epsilon = 0.85$. Since the matrix recession is not uniform (as seen in Fig. 4), the reaction depth was calculated by subtracting the average highest voxel containing matrix in the points on the x-y plane from the highest point in the domain containing a fiber voxel. Error bars indicate the variation in matrix depth within the x-y plane. The values were averaged over approximately 100 time increments to reduce numerical fluctuations. The randomly oriented cylinders exhibit, on the average, the behavior predicted by Eq. 16.

For the matrix-coated case, shown in Fig. 3a in the low Thiele regime, there is no steady state oxidation depth as the entire surface recedes uniformly due to the constant concentration, C_0. However, a transient solution is possible from Eq. 7 and Eq. 8a. Integrating Eq. 8a from 0 to t, the radius of the matrix for

$r_m(t) > r_{f,0}$ is found to be

$$r_m(t) = r_{m,0} - \Omega_m k_m C_0 t \tag{17}$$

When $r_m(t) = r_{f,0}$ at time t_m, the matrix is fully oxidized and the fiber recession begins. Integrating Eq. 7 from t_m to t, the fiber radius is found to be

$$r_f(t) = r_{f,0} - \Omega_f k_f C_0 (t - t_m) \tag{18}$$

for $r_f(t) > 0$ The total recession time for the composite material is found to be

$$t_r = \frac{r_{m,0} - r_{f,0}}{\Omega_m k_m C_0} + \frac{r_{f,0}}{\Omega_f k_f C_0} \tag{19}$$

Simulations in the low Thiele regime were run on a single fiber of radius $r_f = 20\mu\text{m}$ coated with a matrix of $r_m = 10\mu\text{m}$, varying the reactivity contrast between A = 1 and A = 10. The radius evolution in time was compared to the analytical solutions presented in Eq. 17 and Eq. 18 and shown in Fig. 6. The solutions produce good agreement until the radius decreases until the cylindrical shape is no longer accurately captured in the Cartesian grid, around $r_f = 4$ voxels.

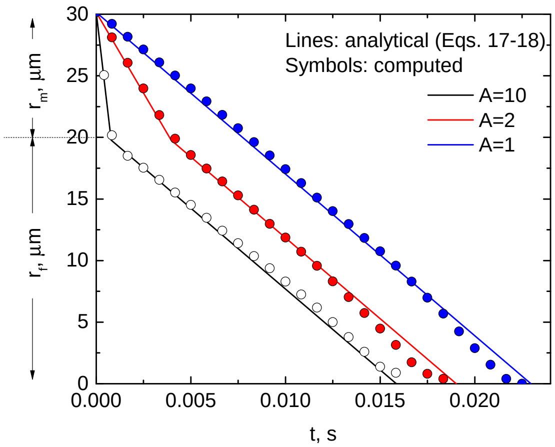

Figure 6: Comparison between the analytical solution in Eq. 17 and Eq. 18 and PuMA simulations at reactivity contrasts of 1, 2, and 10 on a single fiber of $r_f = 20\mu\text{m}$ coated with a matrix of $r_m = 10\mu\text{m}$.

3.2. Simulations on carbon fiber substrates

Simulations were then performed on micro-tomography domains of a real carbon fiber preform in order to observe the effect of resin matrix distribution on a complex geometry. A carbonized phenolic matrix is added to a 520 μm × 520 μm × 1040 μm micro-tomography sample of FiberForm with a reactivity of $5k_f$. For the phenolic-coated case, shown in Fig. 1a, the matrix is applied as a coating over the carbon fiber substrate with a radius of $\approx 2.5\mu\text{m}$, such that the solid volume is doubled.

In the phenolic-filled cases, shown in Fig. 1b, the matrix is evenly distributed in all of the material voids. For an assumed carbon fiber density of $\approx$ 1700 kg/m^2, and an imposed 35% mass fraction of the matrix for both cases, the phenolic-coated case matrix is found to have a density of $\approx$850 kg/m^2. For the phenolic-filled case, the carbonized phenolic matrix density is $\approx$150 kg/m^2. These values vary slightly depending on the sample used, given the small scale of the micro-tomography, the inhomogenous nature of the carbon fiber substrate, and the high uncertainties in manufacturer specifications.

Oxidation was then simulated in each of the three regimes on both the matrix-filled and matrix-coated cases in order to examine the differences in micro-scale oxidation characteristics based on the carbonized phenolic matrix distribution. In both cases, the Thiele number of the simulation was varied between 0.005 and 50, covering the full range of regimes. Figures 7, 8, and 9 show the evolution in time of the oxidation reaction at various Thiele numbers.

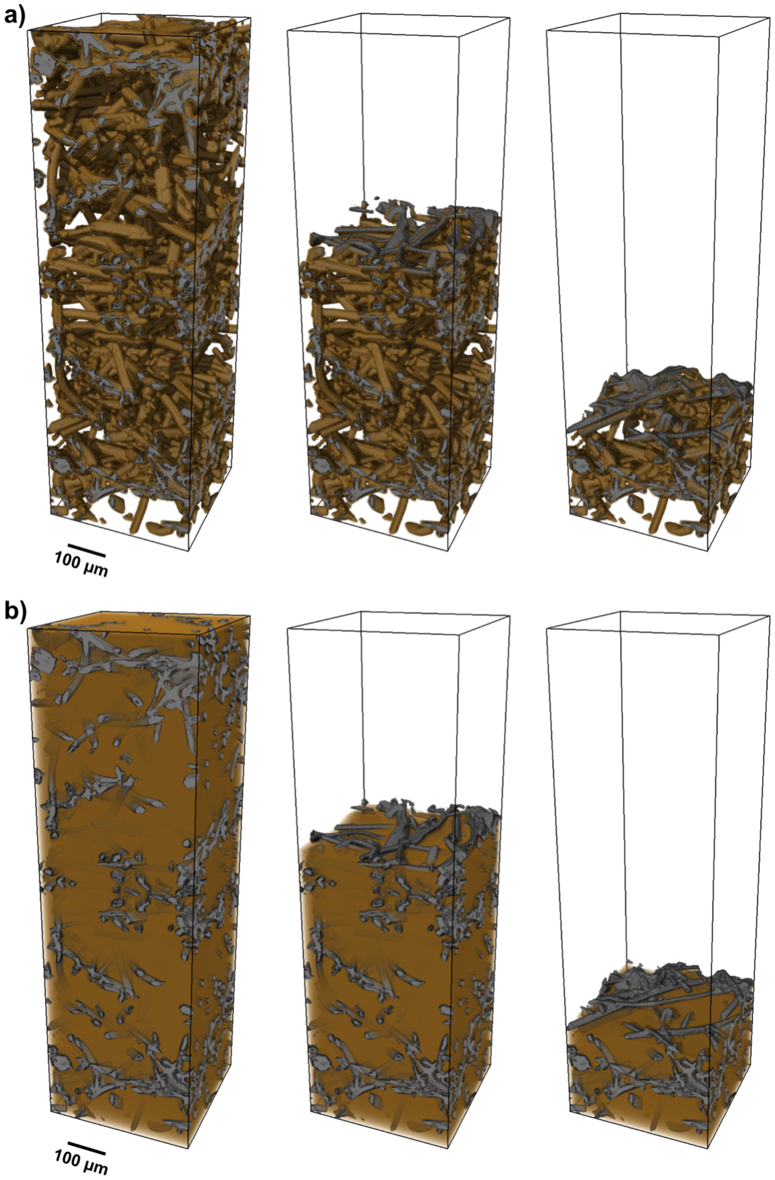

Figure 7: Visualizations of in-depth oxidation in the high Thiele regime ($\Phi = 50$) for a) FiberForm coated in a high density carbonized phenolic matrix (phenolic-coated case) and b) FiberForm filled with a low density carbonized phenolic matrix (phenolic-filled case).

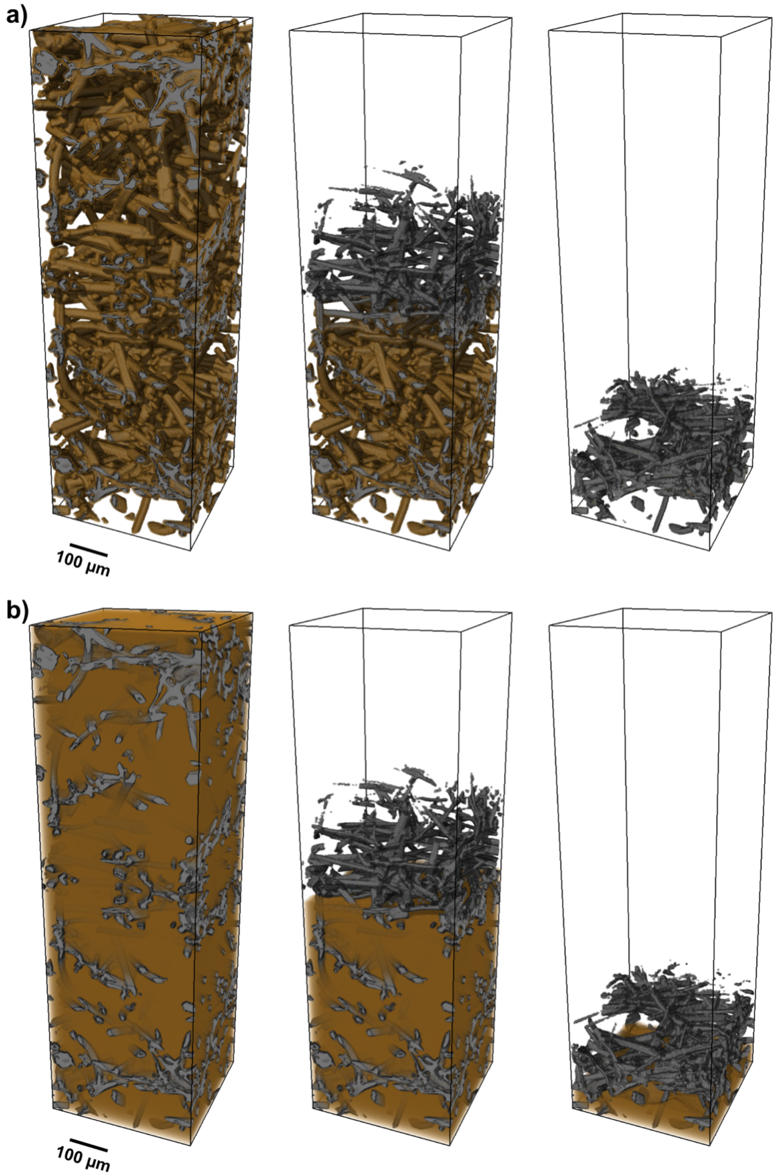

Figure 8: Visualizations of in-depth oxidation in the moderate Thiele regime ($\Phi = 0.5$) for a) FiberForm coated in a high density carbonized phenolic matrix (phenolic-coated case) and b) FiberForm filled with a low density carbonized phenolic matrix (phenolic-filled case).

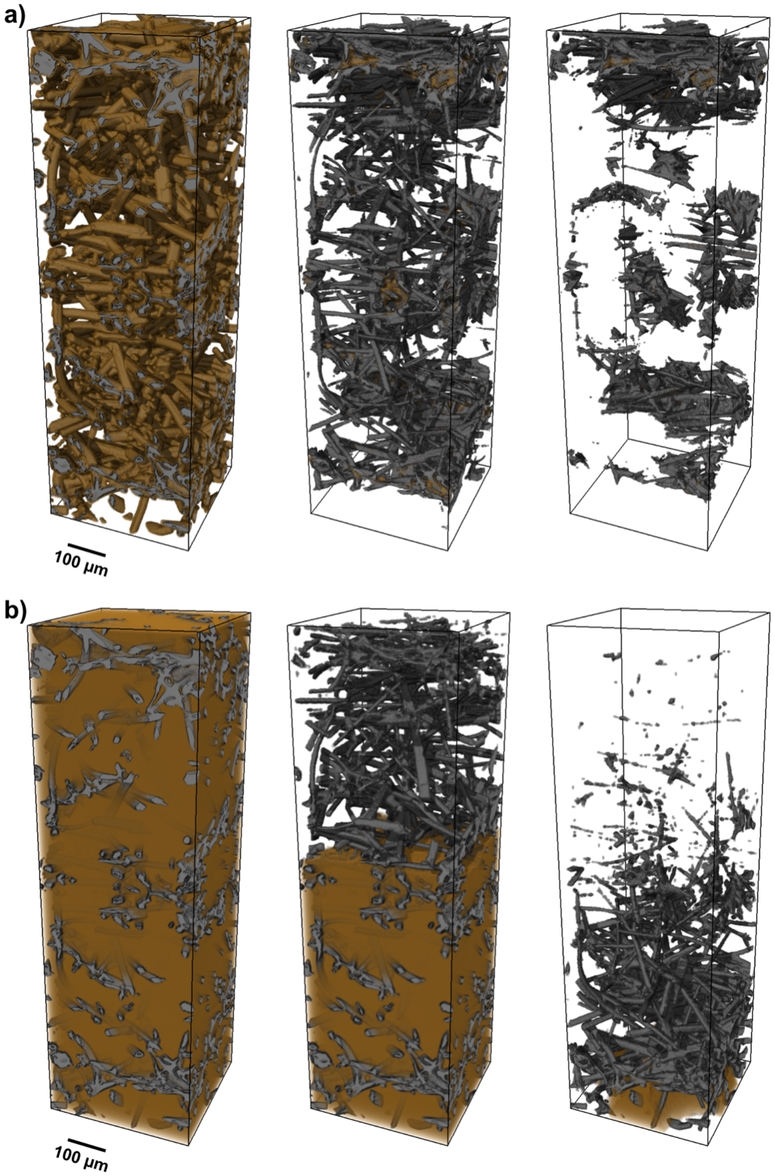

Figure 9: Visualizations of in-depth oxidation in the low Thiele regime ($\Phi = 0.005$) for a) FiberForm coated in a high density carbonized phenolic matrix (phenolic-coated case) and b) FiberForm filled with a low density carbonized phenolic matrix (phenolic-filled case).

As shown by previous studies [8, 14, 24, 25], the oxidation depth is a strong function of the Thiele number. At $\Phi = 50$, both the phenolic-coated and the phenolic-filled cases are fully oxidizing in the surface ablation regime. For a moderate Thiele number, $\Phi = 0.5$, the reactants are able to partially diffuse into the material prior to the oxidation reaction, operating in the mixed regime. For very low Thiele numbers, $\Phi = 0.005$, the reactants fully diffuse into the material and oxidize all exposed surfaces simultaneously, in the volume ablation regime. The in-depth evolution over time of the materials is shown in Fig. 10, which gives the in-depth bulk density change at multiple time steps for the cases presented in Figs. 7-9.

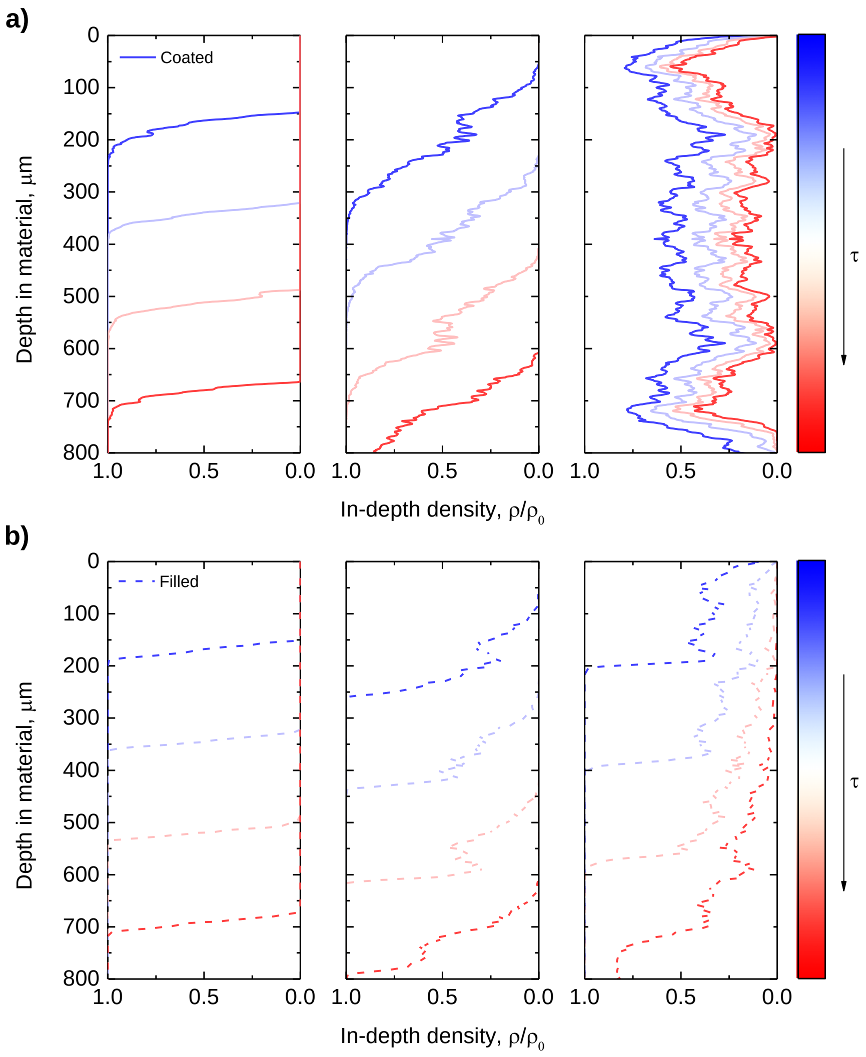

Figure 10: In-depth bulk density change at multiple time steps for a) FiberForm coated in a high density carbonized phenolic matrix (phenolic-coated) and b) FiberForm filled with a low density carbonized phenolic matrix (phenolic-filled). Panels from left to right show decreasing Thiele numbers: $\Phi = 50$, $\Phi = 0.5$, and $\Phi = 0.005$.

In Fig. 10, each simulation is presented at four time steps. The oxidation depth can be measured as the difference in depth between the fully oxidized material ($\rho_z/\rho_0 = 0$) and the virgin material ($\rho_z/\rho_0 = 1$). For all but the $\Phi = 0.005$ phenolic-coated case, the time progression is from the top of the figure to the bottom. For the $\Phi = 0.005$ phenolic-coated case, since the oxidation is in the volume ablation regime, the time progression is from the left to the right of the figure.

It can be seen in Fig. 10 that in high Thiele cases, the simulation quickly reaches steady state, where the recession velocity of the fibers and the phenolic converge, for both matrix distributions. The overall oxidation depth is shallow enough that there is no clear distinction between the oxidation zones of the two phases (carbon fibers and carbonized phenolic) in either the phenolic-coated or phenolic-filled cases. There is little difference in the micro-scale oxidation behavior of the two cases in high Thiele cases.

For a moderate Thiele number, shown in Fig. 10 as $\Phi = 0.5$, a steady state is also reached for both cases. However, the two phases produce two distinct oxidation zones, with noticeable differences beginning to emerge in the oxidation behavior between the phenolic-coated and phenolic-filled cases.

For low Thiele numbers, shown in Fig. 10 as $\Phi = 0.005$, there exist large differences in the oxidation behavior between the two cases, as predicted by the study on ideal fibers in section 3.1. For the phenolic-coated case, the material recedes uniformly in-depth and no steady state is reached. Once the entire coating is oxidized, the recession rate slows significantly due to the decreased reactivity and available surface area. For the phenolic-filled case, matrix recedes and the exposed carbon fibers are uniformly oxidized. For this case, the simulation eventually reaches a steady state.

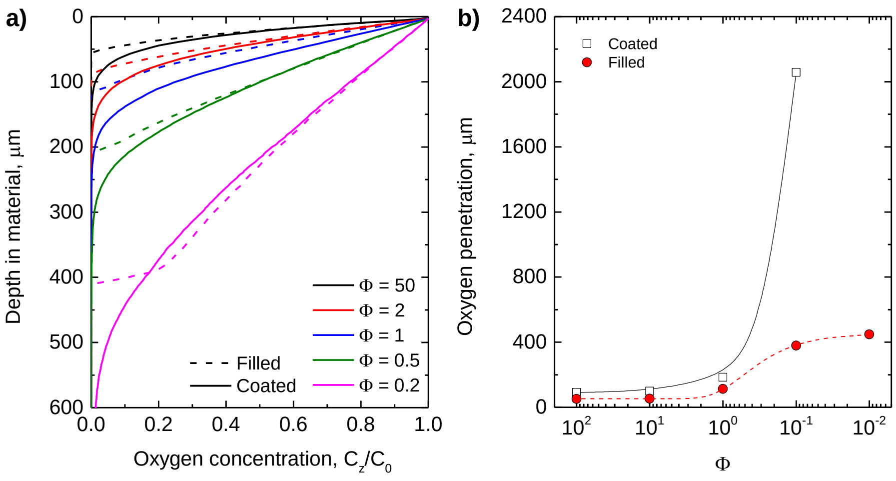

Figure 11: (a) Steady state oxygen concentration in depth at various Thiele numbers for both the matrix-filled and matrix-coated cases. (b) Oxygen penetration depth as a function of Thiele number for the matrix-filled and matrix-coated cases.

Figure 11a shows the in depth oxygen concentration at various Thiele numbers for the two cases, showing that for $\Phi > 2$ the differences in oxygen penetration between the two cases remain relatively small. Figure 11b shows the steady state oxygen penetration depth, with a cutoff at 2% of the reservoir concentration. The domains used in Figs. 7-9 were mirrored in the z direction to reach the necessary depth for the low Thiele cases. We find that the carbonized phenolic distribution results in significant changes in the oxygen penetration in the low Thiele regime. In this regime, a steady state oxidation depth is reached in the matrix-filled case, while the solution diverges in the matrix-filled case as the Thiele number approaches 0. The in-depth oxygen concentration, as well as the available surface area and reactivity of each phase can be used to determine the theoretical steady state oxidation rate of the materials.

The results shown in Figs. 10-11 demonstrate that at high reactivities, there is little difference in the oxidation behavior of carbon phenolic ablators based on the distribution of carbonized phenolic matrix. As the reactivity and Thiele number decrease, large differences develop in the oxidation behavior that are not captured in heritage surface ablation models. Moreover, these differences lead to significant changes in the effective reactive surface area, which is critical for determining oxidation reaction rates. It is important to note that this study only examined the oxidation reaction and did not account for the mass loss due to sublimation or spallation. However, this method has the potential to provide insight into the effect of Thiele number and matrix distribution on the evolution of average fiber radius in the oxidation zone, which may prove useful in the modeling of spallation or other mechanical phenomena.

4. Conclusion

A micro-scale oxidation model was used to study the recession of carbon fibers impregnated with a highly reactive phenolic matrix. Analytical and numerical modeling were carried out on ideal fiber clusters, demonstrating that the oxidation behavior can be predicted on randomly oriented cylinders in the low Thiele regime. Simulations were then conducted on a micro-tomography sample of a carbon fiber preform. It was shown that the oxidation depth is a strong function of the Thiele number, with little effect produced by the matrix distribution at high Thiele number. However, at low Thiele numbers, the carbonized phenolic matrix distribution plays a significant role in the micro-scale oxidation characteristics. These effects must be considered in volume averaged (phenomenological) models, particularly the role of the matrix distribution on the effective reactive surface area and the oxidation depth.

Future work will include the introduction of heat transfer and thermal gradients in order to develop a more physically realistic model. Additionally, a more complex gas model will be included to improve the fidelity of the diffusion and surface reactions, as well as the transport of oxidation products (CO and CO_2) out of the material. Pyrolysis gas transport will also be considered in future works. The production and blowing of pyrolysis gases is likely to affect the diffusion of reactants into the porous media. In addition, pyrolysis gases may react with species from the freestream flow, with oxidation products, as well as with the material itself. The work presented in this paper, as well as future work, will be used to feed next generation volume averaged models, with the ultimate goal of informing future material design.

Acknowledgments

This work was supported by the Entry System Modeling project (M.J. Wright project manager) of the NASA Game Changing Development program. The authors would like to acknowledge T. Sandstrom, C. Henze, D. Ellsworth, and B. Nelson for useful discussions during the development of PuMA. A.A. MacDowell and D.Y. Parkinson are acknowledged for their assistance with tomography measurements. A. Borner and M. Barnhardt are acknowledged for their review of the manuscript. The Advanced Light Source is supported by the Director, Office of Science, Office of Basic Energy Sciences, of the U.S. Department of Energy under Contract No. DE-AC02-05CH11231.

References

[1] K. E. Parmenter, K. Shuman, F. Milstein, C. E. Szalai, H. K. Tran, D. J. Rasky, Compressive response of lightweight ceramic ablators: phenolic impregnated carbon ablator, Journal of Spacecraft and Rockets 38 (2) (2001) 231–236.

[2] K. A. Trick, T. E. Saliba, Mechanisms of the pyrolysis of phenolic resin in a carbon/phenolic composite, Carbon 33 (11) (1995) 1509–1515.

[3] H. K. Tran, C. E. Johnson, D. J. Rasky, F. C. L. Hui, M.-T. Hsu, T. Chen, Y. K. Chen, D. Paragas, L. Kobayashi, Phenolic Impregnated Carbon Ablators (PICA) as Thermal Protection Systems for discovery missions, Tech. Rep. 110440, NASA Technical Memorandum (1997).

[4] A. Martin, S. C. Bailey, F. Panerai, R. S. Davuluri, H. Zhang, A. R. Vazsonyi, Z. S. Lippay, N. N. Mansour, J. A. Inman, B. F. Bathel, et al., Nu-

merical and experimental analysis of spallation phenomena, CEAS Space Journal 8 (4) (2016) 229–236.

[5] R. M. Kendall, E. P. Bartlett, R. A. Rindal, C. B. Moyer, An analysis of the coupled chemically reacting boundary layer and charring ablator: Part I, NASA CR 1060.

[6] J. Lachaud, N. N. Mansour, Porous-material analysis toolbox based on openfoam and applications, Journal of Thermophysics and Heat Transfer 28 (2) (2014) 191–202.

[7] J. Lachaud, G. Vignoles, A Brownian Motion Technique to Simulate Gasification and its Application to C/C Composite Ablation, Computational Materials Science 44 (6) (2009) 1034–1041.

[8] J. Lachaud, I. Cozmuta, N. Mansour, Multiscale Approach to Ablation Modeling of Phenolic Impregnated Carbon Ablators, Journal of Spacecraft and Rockets 47 (6) (2010) 910–921.

[9] J. Lachaud, N. N. Mansour, Microscopic scale simulation of the ablation of fibrous materials, in: 48th AIAA Aerospace Sciences Meeting Including the New Horizons Forum and Aerospace Exposition, AIAA Paper 2010-984, 2010.

[10] N. N. Mansour, F. Panerai, A. Martin, D. Y. Parkinson, A. MacDowell, A. Haboub, T. A. Sandstrom, T. Fast, G. L. Vignoles, J. Lachaud, A new approach to light-weight ablators analysis: from micro-tomography measurements to statical analysis and modeling, in: 44^{th} AIAA Thermophysics Conference, AIAA Paper 2013-2768, San Diego, CA, USA, 2013.

[11] A. A. MacDowell, D. Y. Parkinson, A. Haboub, E. Schaible, J. R. Nasiatka, C. A. Yee, J. R. Jameson, J. B. Ajo-Franklin, C. R. Brodersen, A. J. McElrone, X-ray micro-tomography at the advanced light source, Proc. SPIE 8506, Developments in X-Ray Tomography VIII (2012) 850618–14.

[12] J. Baruchel, J.-Y. Buffiere, E. Maire, X-ray tomography in material science, 2000.

[13] E. Maire, On the application of x-ray microtomography in the field of materials science, Advanced Engineering Materials 3 (8) (2001) 539–546.

[14] J. C. Ferguson, F. Panerai, J. Lachaud, A. Martin, S. C. Bailey, N. N. Mansour, Modeling the oxidation of low-density carbon fiber material based on micro-tomography, Carbon 96 (2016) 57–65.

[15] C. Park, Effects of atomic oxygen on graphite ablation, AIAA Journal 14 (11) (1976) 1640–1642.

[16] S. J. Poovathingal, T. E. Schwartzentruber, V. Murray, T. K. Minton, G. V. Candler, Finite-rate oxidation model for carbon surfaces from molecular beam experiments, AIAA Journal 55 (5) (2017) 1644–1658.

[17] J. Lachaud, N. Bertrand, G. L. Vignoles, G. Bourget, F. Rebillat, P. Weisbecker, A theoretical/experimental approach to the intrinsic oxidation reactivities of C/C composites and of their components, Carbon 45 (14) (2007) 2768–2776.

[18] A. Borner, F. Panerai, N. N. Mansour, DSMC study of carbon fiber oxidation in ablative thermal protection systems, in: 45th AIAA Thermophysics Conference, 2015, p. 3370.

[19] W. E. Lorensen, H. E. Cline, Marching cubes: A high resolution 3D surface construction algorithm, SIGGRAPH Comput. Graph. 21 (4) (1987) 163–169.

[20] J. Salles, J. F. Thovert, P. M. Adler, Deposition in porous media and clogging, Chemical Engineering Science 48 (1993) 2839–2858.

[21] J. Lachaud, Y. Aspa, G. L. Vignoles, Analytical modeling of the steady state ablation of a 3D C/C composite, International Journal of Heat and Mass Transfer 51 (9–10) (2008) 2614–2627.

[22] L. Dagum, R. Menon, OpenMP: an industry standard API for shared-memory programming, Computational Science & Engineering, IEEE 5 (1) (1998) 46–55.

[23] OpenMP Architecture Review Board, OpenMP application program interface version 3.0 (May 2008).

[24] F. Panerai, J. C. Ferguson, J. Lachaud, A. Martin, M. J. Gasch, N. N. Mansour, Micro-tomography based analysis of thermal conductivity, diffusivity and oxidation behavior of rigid and flexible fibrous insulators, International Journal of Heat and Mass Transfer 108 (2017) 801–811.

[25] F. Panerai, J. Ferguson, J. Lachaud, A. Martin, M. J. Gasch, N. N. Mansour, Analysis of fibrous felts for flexible ablators using synchrotron hard X-ray micro-tomography, in: 8th European Symposium on Aerothermodynamics for Space Vehicles.